多次元評価手法の統合化による都市施地震脆弱性診断手法の高度化

AUTHOR(S):

中島, 正愛; 田中, 仁史; 岩田, 知孝; 澤田, 純男; 松波, 孝治; 吹田, 啓一郎; 田村, 修次

CITATION:

中島, 正愛 ...[et al]. 多次元評価手法の統合化による都市施地震脆弱性診断手法の高度化. 京都大学防災研究所年報. C 2006, 49(C): 9-22

ISSUE DATE:

2006-04-01

URL:

http://hdl.handle.net/2433/26670

京都大学防災研究所年報 第 49 号 C 平成 18 年 4 月
Annuals of Disas. Prev. Res. Inst., Kyoto Univ., No. 49 C, 2006

Advanced Techniques for Evaluating Vulnerability of Urban Infrastructure by Integrating Multiple Evaluation Indexes

Masayoshi NAKASHIMA, Hitoshi TANAKA, Tomotaka IWATA,
Sumio SAWADA, Keiichiro SUITA, and Shuji TAMURA

Synopsis

It is essential for disaster prevention to quantify the earthquake vulnerability of urban infrastructures in consideration of their life cycle. As part of a five-year study on this subject, presented in this article are: the refinement of prediction of strong motions, examinations into actual performance of nonstructural components, rational evaluation of RC building structures in consideration of foundation-structure interaction, effects of total earth pressure on pile forces, and development of a systematic procedure for the estimation of life-cycle cost for large-scale lifeline network.

Keywords: strong ground motion, performance of nonstructural components, foundation-structure interaction, earth pressure, life cycle cost

1. Introduction

The rational evaluation of earthquake vulnerability of our urban infrastructures require accurate prediction of strong motions, thorough characterization of the performance of structures, soils, structure-building system, and soil-structure systems, and development of methodologies that can effectively consider the life-cycle cost/performance of the structures and systems. This is a five-year project being undertaken within the scope of Center of Excellence for Natural Disaster Science and Disaster Reduction, implemented by the Disaster Prevention Research Institute, Kyoto University. Achievement of fiscal 2005 is summarized in what follows.

2. Strong Ground Motion Prediction for Design Ground Motion

A large shallow crustal earthquake jolted western off-shore of Fukuoka Prefecture, northern Kyushu, Japan, it brought severe strong ground motions to the near-source region, such as Genkai Island, Shikanoshima Island, and the central district of Fukuoka City. To understand generation of strong ground motions in near-source area, we have analyzed strong motion data of this event. At first, the source process of the 2005 West Off Fukuoka Prefecture earthquake is studied using the strong motion seismograms obtained by Japanese nation-wide strong motion seismograph networks, K-NET and KiKnet. These networks are installed and operated by the National Research Institute for Earth Science and Disaster Prevention (NIED). Second, we also evaluated strong motion generation area (SMGA, Miyake et al. 2003) in the wide-frequency range by the empirical Green's function method. We also discuss the relationship between the asperity by waveform inversion and SMGA. Finally, a three-dimensional ground motion simulation using a finite difference method reveals the spatial variation of ground motions in the near-source area.

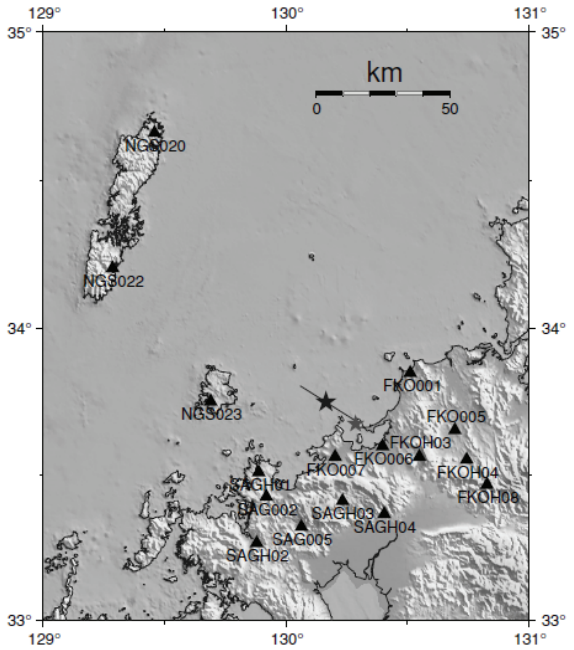

Fig. 1. Map showing studied area. The black and gray stars indicate the epicenters of the mainshock and the largest aftershock, respectively. The solid line shows the projection of the fault plane of the mainshock. Solid triangles indicate the locations of strong motion stations used for the waveform inversion.

2.1 Waveform inversion of the 2005 West Off Fukuoka Prefecture earthquake by strong motion data

The source rupture process of the mainshock is estimated by the kinematic linear waveform inversion with multiple time windows (Sekiguchi et al. 2000). This methodology is originally based on the technique developed by Hartzell and Heaton (1983). A planar fault plane model is assumed referring to the aftershock distributions. The length and width of the fault plane are 26 km and 18 km, respectively. According to the moment tensor solution by the F-net (NIED), the strike and dip of the fault plane are assumed to be 122, and 87degrees, respectively. The rupture starting point is fixed at the hypocenter location (33.75N, 130.16E, 14 km) determined by the Institute of Seismology and Volcanology, Faculty of Sciences, Kyushu University (ISV). Fig. 1 shows the assumed fault plane and strong motion stations using waveform inversion. We Data at nine stations of the K-NET and seven stations of the KiK-net are used for the waveform inversion (see Fig. 1). For the KiK-net stations, uphole seismograph data is used. From among many available stations, stations which have enough quality to retrieve the source process were selected by the visual inspection. Observed digital acceleration data are integrated into the ground velocities in the time domain with a filter between 0.05 and 1.0 Hz. We inverted 16 s of the *S*-wave portion from 1 s before the direct *S*-wave arrival.

Fig. 2 shows the final slip distribution on the fault surface estimated by the inversion. The rupture front propagation velocity, which triggers the rupture of the first time window, was selected to be 2.1 km/s. This is approximately equal to 60% of the shear-wave velocity at the depth of the rupture. The rupture mainly propagated to the southeastward. The asperity or large slip area with the maximum slip of 3.2 m was observed at southeast of the hypocenter, and relatively smaller slip was observed in the vicinity of the hypocenter. The slip direction is almost pure left-lateral strike slip. Fig. 3 shows the comparison between the observed and synthesized ground velocities in 0.05–1.0 Hz. The synthesized waveforms match well the observed ones at most stations. Fig. 4 shows the temporal rupture progression on the fault. The rupture started from the hypocenter with the small slip velocity, and the entire rupture continued for approximately 10 s. The asperity ruptured at approximately 3.5 s after the initiation of the rupture (Asano and Iwata, 2006).

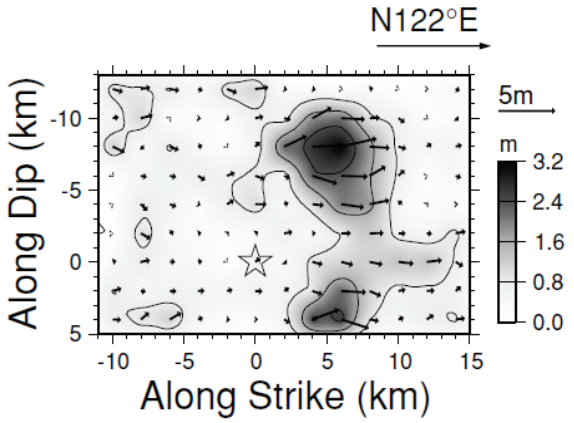

Fig. 2. Final slip distribution of the mainshock estimated from the inversion. The open star indicates the rupture starting point. The allows show the slip vectors of the hanging wall relative to the foot wall. The interval of contours is 0.8 m.

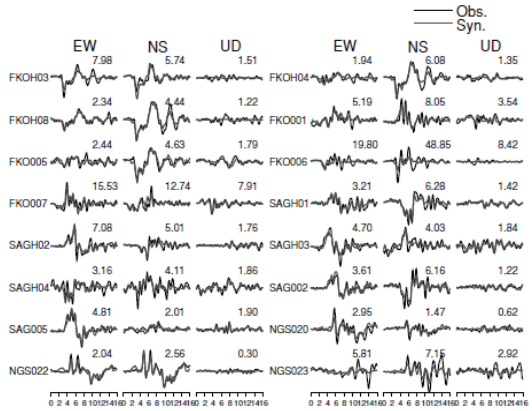

Fig. 3. Comparison between observed (black traces) and synthesized (gray traces) velocity waveforms of the mainshock. The maximum amplitude of each component of observed waveforms are shown above each trace in cm/s. The horizontal axis is time (s).

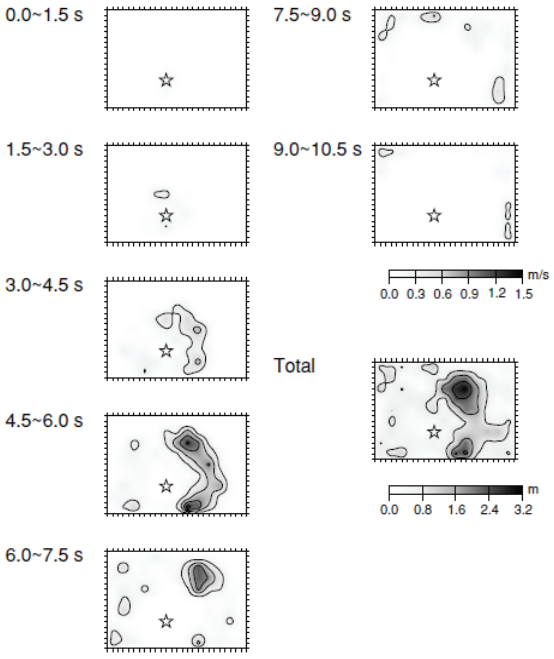

Fig. 4. Snapshots of the temporal rupture progression on the fault at time step of 1.5 s. The contour interval of the slip velocity is 0.3 m/s. The open star indicates the rupture starting point. The figure at bottom right shows the final slip distribution.

2.2 Estimation of strong motion generation area by the empirical Green's function method

In this section, we estimated strong motion generation area (SMGA) source model which is responsible for broadband (0.2, 0.3-10 Hz) strong motions of the 2005 west off Fukuoka prefecture earthquake. Model parameters to be estimated for SMGA are the length, the width, the rise time, the rupture starting time relative to the initial rupture time, the rupture starting subfault of the SMGA, and its relative location from the hypocenter. The genetic algorithm (GA) was employed for these parameter search. Search ranges of model parameters are 0.3–15 km for the length and the width, 0.03–2.1 s for the rise time, 1.0–5.0 s for the delay time of the SMGA rupture, and the 0–10 km from the hypocenter along the strike and up-dip direction for the SMGA rupture starting point. Ten GA search trials were performed to confirm the robustness of the solutions. We kept the rupture velocity in the SMGA constant during each GA search. We tried four rupture velocity, 3.15, 2.8, 2.45, and 2.1 km/s. When the rupture velocity is 3.15 km/s, or 90% of the *S*-wave velocity, we obtained the models which gave the smaller residual value than the search with any other rupture velocity. Location of the estimated SMGA is shown in Fig. 5 with final slip distribution obatained in 2.1. The SMGA seems to be matched to the large slip area. The SMGA rupture started from a point 6km along strike and 4 km up-dip away from the hypocenter with 3.3 s delay to the initial rupture time, and propagated upward and northwest. The size of the estimated SMGA follows the self-similar empirical formula of the asperity size derived by Somerville et al. (1999). The stress drop of the mainshock SMGA is calculated to be 10.7 MPa, which is average stress parameter on the asperity for the crustal earthquakes (Suzuki and Iwata 2006).

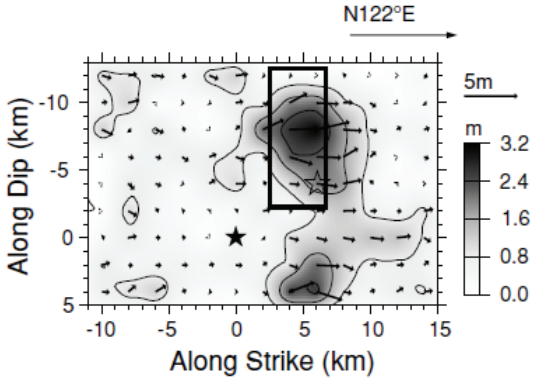

Fig. 5. Comparison of the SMGA and final slip distribution. Rectangle is the estimated SMGA with open star indicating the rupture starting subfault. Black star is the hypocenter of the mainshock.

2.3 Ground motion simulation in the source area

To see the spatial variation of strong ground motions in the near-source region, a three-dimensional ground motion simulation is carried out with the use of the finite difference method. Three sedimentary layers (VS = 600, 1100, 1700 m/s) are assumed above the bedrock. Material parameters assumed for this layered underground structure model basically follow that of Nakamichi and Kawase (2002), and those parameters of each layer. The target frequency range of the calculation is up to 1.0Hz. The simulated distribution of maximum horizontal velocity at surface is shown in Fig. 6. The area where large ground motion was expected from the simulation extended to the southeastward from the fault because of the relatively deep basin structure in the center of Fukuoka City as well as the forward directivity effect of the fault rupture. Genkai Island and Shikanoshima Island are located in the area with large ground motion above the fault. The localized area with relatively large ground motions were also expected at the northwest of the hypocenter and around the hypocenter.

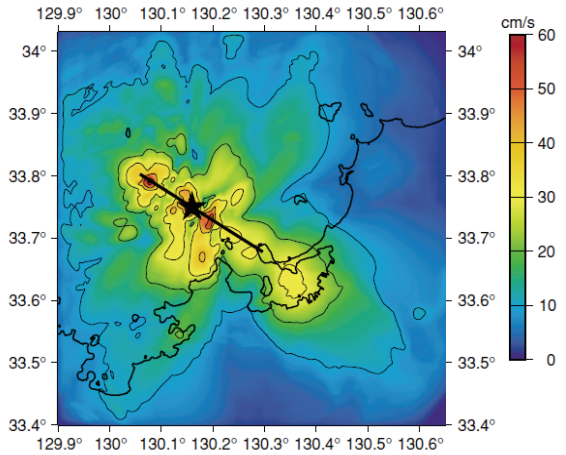

Fig. 6. Spatial distribution of simulated maximum horizontal velocity surface. The interval of contours is 10 cm/s.

3 Performance of Nonstructural Components in Earthquake Conditions

3.1 Problem Statement and Objectives

"Performance-based engineering" has become a standard norm in the research, development, and practice of earthquake engineering, particularly after the 1994 U.S. Northridge and 1995 Hyogoken-Nanbu (Kobe) earthquakes, for example (for example, Performance (1995); Recommended 2000; NEHRP 2000; Notification 2000; Midorikawa et al. 2003). Relevant themes of challenges range from the characterization of strong motions and their effects on the structural response; quantification of multiple levels of performance associated with functionality, damage, and safety limit states; and examinations of the interactions among various nonstructural components and building contents with building performance, among many others. In conjunction particularly with functionality, the past earthquake damage disclosed the significant effect of nonstructural components such as exterior cladding, interior partitions, windows, building contents on the performance. Data on nonstructural performance, however, are very scarce primarily because of the necessities of implementing the test in the full-scale. To obtain quantitative data on seismic performance of nonstructural components, a full-scale test was carried out, in which ALC panels commonly used as exterior cladding in Japanese steel buildings were tested.

3.2 Test Structure

The test structure was a three-story, two-bay by one-bay steel moment frame as shown in Fig. 7, having a plan dimension of 12 m in the longitudinal direction by 8.25 m in the transverse direction. The structure was designed following the most common design considerations exercised in Japan for post-Kobe steel moment frames. That is, the columns were made of cold-formed square-tubes, beams were made of hot-rolled wide-flanges and through-diaphragm connection details were adopted in which short brackets were shop-welded to the columns. The columns with short brackets were transported to the test site, and they were connected horizontally to beams by high-strength bolts. Metal deck sheets were placed on top of beams, with studs welded to the beam top flanges through the metal deck sheets. Wire-meshes were placed above the metal deck sheets, and concrete was placed on site. Fabrication and construction procedures adopted for the test structure faithfully followed those exercised in recent practice (Nakashima et al. 1998).

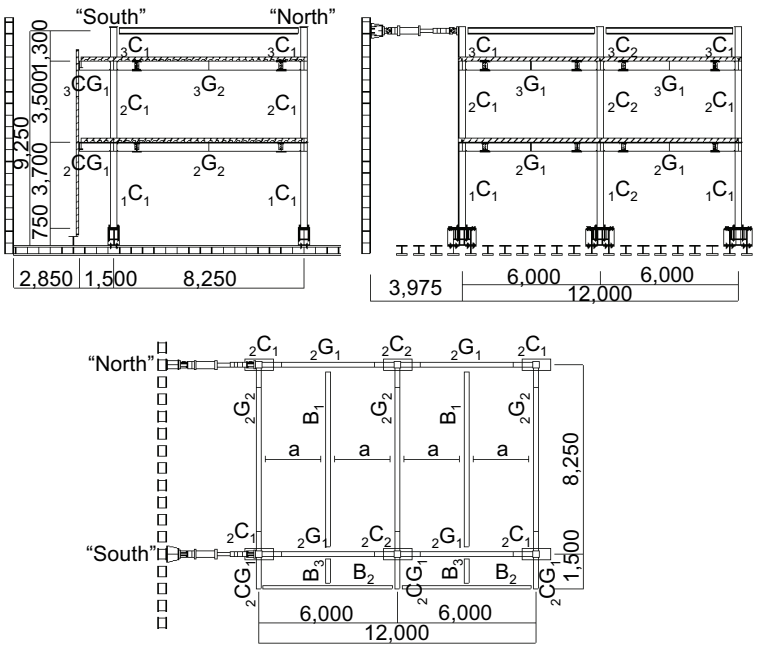

Member		Section	Member		Section (Stud bolt)
Column	$_1C_1$	❑-300x9	Beam	$_2G_1$	H-400x200x9x16 (19φ h=110 Single@200)
	$_1C_2$	❑-300x12		$_2G_2$	H-400x200x9x16 (19φ h=110 Single@200)
	$_2C_1$	❑-300x9		$_3G_1$	H-400x200x9x16 (19φ h=110 Single@200)
	$_2C_2$	❑-300x9		$_3G_2$	H-400x200x9x16 (19φ h=110 Single@200)
	$_3C_1$	❑-300x12		$_2CG_1$	H-400x200x8x13 (19φ h=110 Single@200)
	$_3C_2$	❑-300x16		$_3CG_1$	H-400x200x8x13 (19φ h=110 Single@200)
Anchor bolt	M33	length=740 (110)		B_1	H-400x200x8x13 (16φ h=110 Single@300)
	M36			B_2	H-300x150x6.5x9 (No)
Base plate		50x475x475		B_3	H-200x100x5.5x8 (16φ h=110 Single@300)
Mesh		6φ 150x150		a	H-200x100x5.5x8 (No)

Unit: mm

Fig. 7 Plan and elevation of test structure (unit: mm)

The two planes placed in parallel in the longitudinal direction were nearly identical, but one plane, called the "South" plane, had a floor slab extended on the exterior side by 1.5 m, while the other plane, called the "North" plane, had a floor slab that terminated at the beam end (Fig.7). This overhang was designed to help estimate the effects of RC floor slabs from the difference in resistance between the two planes. The columns were extended to the approximate mid-height of the third story, at which level steel braces were connected horizontally to the columns by high-strength bolts through gusset plates. Two quasi-static jacks, one in each longitudinal plane, were placed at this level, as shown in Fig.7. The test structure was equipped with the exterior walls installed during the test. ALC (autoclaved lightweight concrete) panels, which are very popular in Japanese steel buildings, were placed at some stages of loading to examine the effects of exterior walls on the hysteretic behavior of the test structure. The ALC panels were installed along the floor edge of the "South" plane (the one with the overhang) (Fig. 8) (Matsumiya et al. 2004).

3.3 Loading Program

As shown in Fig.7, two quasi-static jacks were arranged for horizontal loading. Each jack was placed at one end of the test structure and at the mid-height of the third story. An identical displacement was applied to both jacks. Fig. 9 shows the loading program used in the test. Quasi-static cyclic loading with increasing displacement amplitudes was adopted, and either two or three cycles were repeated for each amplitude. The displacement was controlled in terms of the overall drift angle, defined as the horizontal displacement at the loading point relative to the loading height of 8.5 m. Overall drift angles of 1/200 rad, 1/100 rad, 1/75 rad,

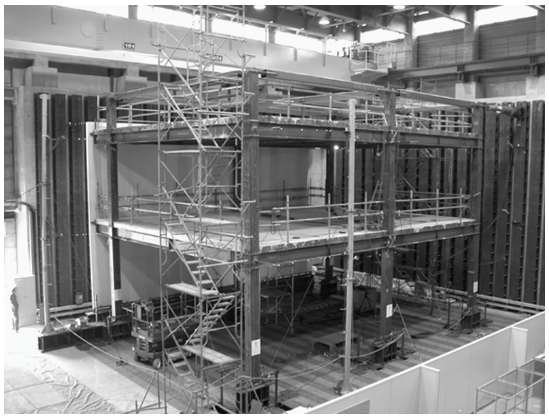

Fig. 8 Overview of test structure (with ALC panel on the back side)

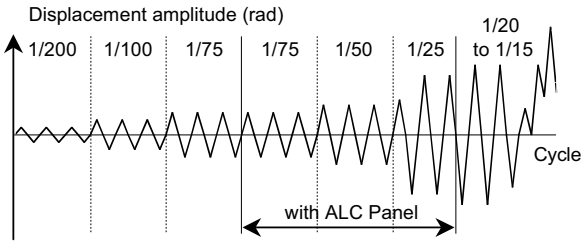

Fig. 9 Lateral displacement program

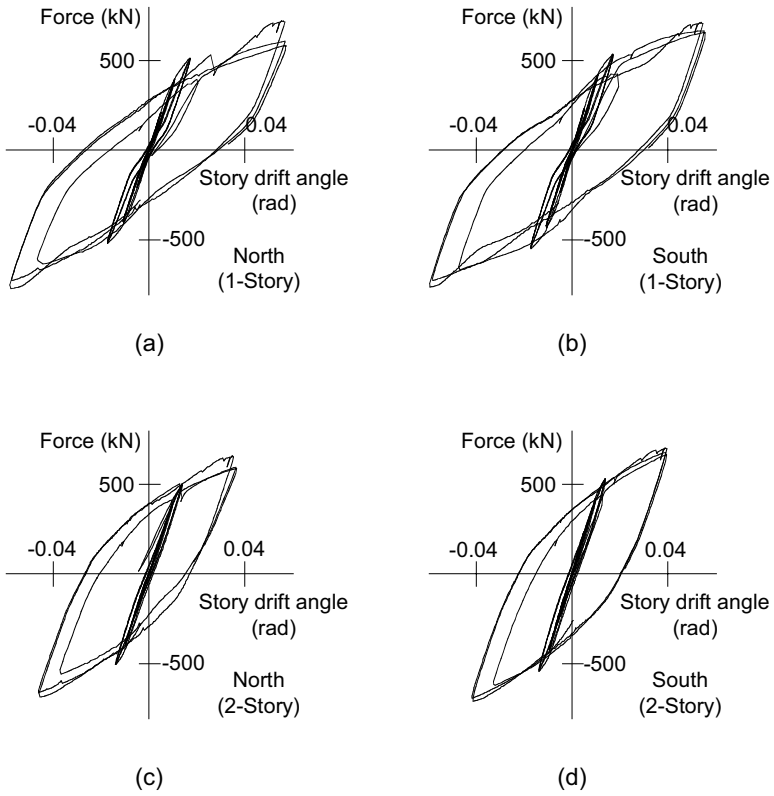

Fig. 10 Story shear versus story drift angle relationships up to 1/20 overall drift: (a) First story in "North" plane; (b) First story in "South" plane; (c) Second story in "North" plane; (d) Second story in "South" plane

1/50 rad, 1/25 rad, and 1/20 rad were adopted. A computer controlled on-line test system was used for the test. The system was able to ensure flexible control in either the displacement or force mode as well as to conduct fully automatic loading and measurement. The full details of the control system are described in (Nakashima et al. 1995; Nakashima and Liu 2004).

3.4 Test Results and Findings

Fig. 10 shows the story shear versus story drift angle relationships up to the overall drift angle of 1/20. The relationships are presented with respect to the story (the first and second stories) and plane (the "North" and "South" planes). The story shear force was the load applied by the jack placed in the concerned plane. During the test for the overall drift angle equal to and greater than the 1/75 amplitude, beams, panel-zones, and column bases developed small plastic deformations, which indicates balanced participation of individual components to the overall deformations. Pinching behavior in the second and third cycles relative to the first cycle was notable for the 1/75 amplitude and greater.

This was primarily due to yielding and progress of plastic deformations of the anchor bolts. Such yielding was intended in the design of the test structure.

In the 1995 Kobe earthquake, many damage instances were reported to ALC panels, including cracks, separations along the edges, and drops to the ground (Reconnaissance 1995). Most of the damaged panels were attached to the frame using old attachment details that could not accommodate sufficient rigid-body movement to the panels. For the installation of ALC panels in the test, post-Kobe attachment details were adopted. The details accommodate large rigid rotations of the panels thanks to the slotted holes of attachment angles. The panels were attached to the test frame after loading with the initial three cycles of the 1/75 amplitude (see Fig.9). The frame attached with the panels was loaded for additional three cycles of the 1/75 amplitude, three more cycles of the 1/50 amplitude, and three more cycles of the 1/25 amplitude.

Practically no damage was detected in the panels throughout the loading, and interaction between the panels and frames was negligible. This performance, i.e., nearly no damage to a drift angle of 1/25, was beyond the expectation before the test in that the associated technical data provided by the supplier of the panels suggested a drift angle of 1/50 for guaranteed safety. Although not damaged, the ALC panels were removed at the end of loading with the 1/25 amplitude due to a fear of serious damage to the test facility during the succeeding loading with larger deformations. The details on this issue are presented in (Matsumiya et al. 2004).

4. Lateral Force Resisting Mechanism of a Multi－Story Shear Wall and Peripheral Members

4.1 Introduction

In current design procedures (AIJ 1992; Paulay and Priestley 1992), cantilever structural walls are normally assumed to stand on a solid foundation, and foundation beams, slabs and piles are designed separately without considering their interactions. This study aims to experimentally clarify the variation of the lateral load resisting mechanisms considering the interaction between a shear wall, a foundation beam, slabs and piles, and to establish more rational design procedures for each structural component. This experimental study was conducted by Masanobu Sakashita, Susumu Kono, Hitoshi Tanaka and Fumio Watanabe. A full report on this study is to be submitted to Second International fib Congress held in Naples, Italy, from June 5-8, 2006.

4.2 Specimens

The specimen configuration was determined from typical fourteen-story residential buildings in Japan. The assemblage consisting of the lowest three floors of a shear wall with a foundation beam, the first floor slab, and two piles in the transverse direction was scaled to 1/4. Fig. 11 shows specimen configuration. The monolithic action between foundation beam and peripheral members, such as a shear wall, slabs and piles, is expected and it restricts the damage of the foundation beam. The amount of longitudinal reinforcement in the foundation beam was set smaller than the requirement calculated from the Japanese design guideline (BCJ 1999).

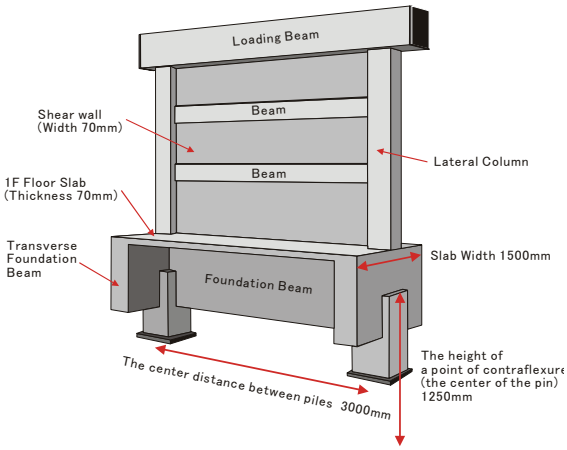

Fig.11 Specimen configuration

4.3 Test Setup

As shown in Fig. 12, lateral load, Q, was applied statically through a 1000kN horizontal jack to the loading beam. Two 2000kN vertical jacks were adjusted to create appropriate column axial forces, N1 and N2, which are a liner function of lateral load, Q, to simulate loading conditions of the prototype fourteen-story shear wall system under earthquakes.

At the roller support, 0.7Q was applied horizontally to the pile on the compressive side and 0.3Q was applied to the piles on the tensile side by a 1000kN jack in the opposite direction to the 1000kN horizontal jack. The load was applied two cycles at each prescribed load

stage until the first story drift angle went to 0.1%, then the displacement control was used with two cycles at each prescribed displacement.

In this experiment, it is difficult to measure only the drift angles of the shear wall because of the rotation and the deformation of the foundation. So they were calculated from the flexural deformation and the shear deformation of the shear wall and the relative sliding of the shear wall base. They were measured with the multiple displacement gauges placed at the shear wall.

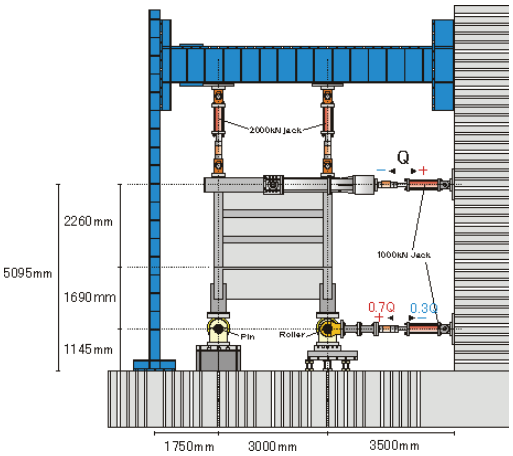

Fig. 12 Loading system

4.4 Observed Damage

Fig. 13 (a) to (c) show cracks and other damage after testing and diagrammed illustration of the damage at the ultimate state. Flexure-shear cracks of the shear wall penetrated the slabs transversely and developed to the foundation beam. Fig. 13 (c) shows damage of the shear wall base. On the west side longitudinal bars of the column buckled and from the midspan of the shear wall to the east column vertical bars of the shear wall fractured.

In this experiment, concrete crushing was hardly observed at the base of the columns. At the ultimate state, the shear wall separated along the flexure-shear cracks that developed to the foundation beam involving the parts of the foundation beam, the pile, the transverse foundation beam and the slabs. In consequence, the reduction of the lateral load didn't occur until loading test was finished, as can be seen from Fig. 14.

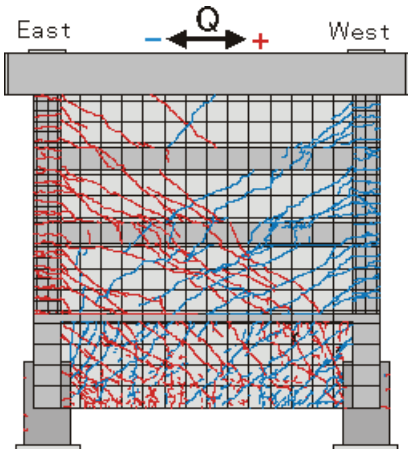

(a) Crack distribution

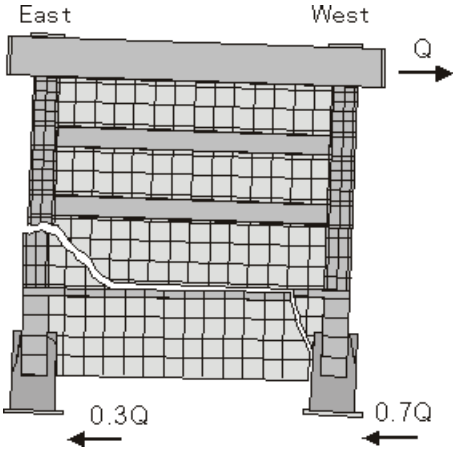

(b) Diagrammic illustration of the damage at the ultimate state

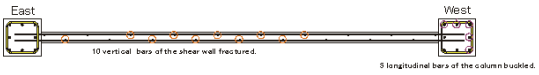

(c) Damage of the shear wall base

Fig.13 Cracks and other damage after testing and diagrammic illustration of the damage

4.5 Conclusion

One 1/4-scale cantilever structural wall systems was tested to clarify the variation of the lateral load resisting mechanisms considering the interaction between a shear wall, a foundation beam, slabs and piles. The main conclusions can be summarized as follows.

· Flexure-shear cracks of the shear wall penetrated the slabs transversely and developed to the foundation beam. At the ultimate state, the shear wall separated along these cracks involving the parts of the foundation beam, the pile, the transverse foundation beam and the slabs. Contrary to the design, the

yielding of the shear wall preceded the yielding of the foundation beam. These clarified monolithic action between a foundation beam and peripheral members.

· Strain distributions of longitudinal reinforcement in a foundation beam from experiment and analysis show the shear transfer mechanism clearly. In the analysis, it is assumed that the foundation beam is subjected to moment from the piles (Mp), moment (Mq) and axial force (N) due to lateral force Q, acting on the upper edge of the foundation beam, and moment due to vertical longitudinal bars in the shear wall (Mw). Analytical part was not shown in this paper due to the limit of the given space.

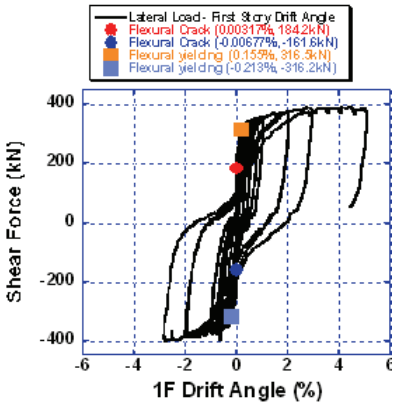

(a) Characteristic points of the shear wall

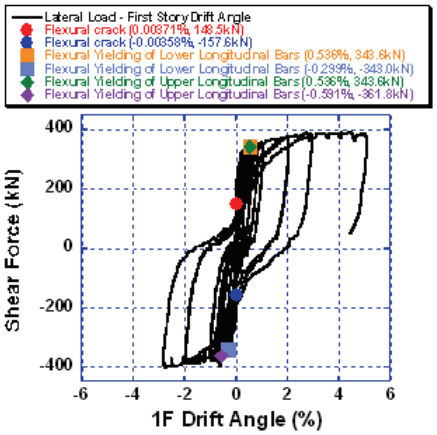

(b) Characteristic points of the foundation beam

Fig. 14 Lateral load – first story drift relation

5. Effects of Superstructure Inertia and Total Earth Pressure on Pile Forces

5.1 Objectives

To qualitatively investigate the effects of inertial and kinematic forces, several series of large-scale shaking table tests were conducted on soil-pile-structure systems with dry sand (Tokimatsu et al. 2004) and with saturated sand (Tamura et al. 2000). Total earth pressure acting on the embedded footing was evaluated in the tests. The objective of this paper is to examine the effects of the total earth pressure on the piles forces in both non-liquefaction and liquefaction tests.

5.2 Model Preparation

This paper presents the earth pressure acting on an embedded footing based on the results of two shaking table tests with dry sand (case DBL after Tokimatsu et al. 2004) and with saturated sand (case SBL after Tamura et al. 2000), as shown in Fig. 15. The tests were performed at NIED (National Research Institute for Earth Science and Disaster Prevention) in Tsukuba, Japan, using a large-scale laminar shear box of 4.6 or 6.1 m in height, 3.5 m in width and 12.0 m in length (shaking direction) mounted on the shaking table. The soil used for case DBL was Nikko Sand. The relative density of the dry sand deposit was about 80%. The soil profile in case SBL consists of two layers including a 4.5 m layer of Kasumigaura sand with a shear wave velocity of 90 m/s, which is underlain by a 1.5 m layer of gravel with Vs = 230 m/s. The water level was located at about GL-0.5 m. The relative density of the saturated sand deposit was about 35-50%.

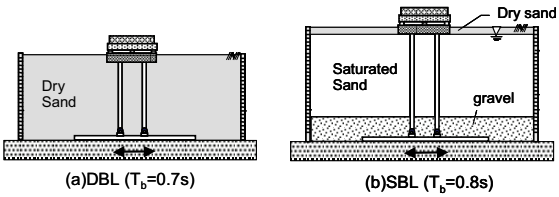

Fig. 15 Test models

A 2x2 steel pile was used for all the tests. The piles had a diameter of 16.5 cm, a thickness of 0.37 cm and a flexural rigidity EI of 1259 kNm^2. The pile heads were rigidly linked to the footing, while their tips were connected to the laminar shear box by hinges. The footing was modeled with a rigid steel box of 2.5 m (length) x 1.8 m (width) x 0.6 m (height) and embedded 0.5 m in the dry sand. The mass of the superstructure was 14200 kg and that of the footing was 2100 kg. The natural period of the superstructure was about 0.7 s for case DBL, which was longer than the natural period of the ground. The natural period of the superstructure

in case SBL was about 0.8 s, which is longer than that of the ground before liquefaction but shorter than that after liquefaction. All the tests were excited by RINKAI92, which is a synthesized ground motion for the Tokyo Bay area. The amplitude of the motion was scaled to 240 cm/s^2.

5.3 Effects of Superstructure Inertia and Total Earth Pressure on Pile Forces

Fig. 16 shows superstructure inertia, total earth pressure and shear force at pile head when the bending moment at pile head reaches its maximum in cases DBL and SBL. The superstructure inertia and the total earth pressure in case DBL are larger than those in case SBL. On the other hand, the shear force at pile head in case DBL is smaller than that in case SBL. The difference between cases DBL and SBL is the phase between the superstructure inertia and the total earth pressure. The total earth pressure is out of phase by 180 degrees with the superstructure in case DBL. The total earth pressure is in phase with the superstructure in case SBL. Therefore, the shear force at pile head in case DBL is smaller than that in case DBL. This indicates that the phase between superstructure inertia and total earth pressure is the key to discussing the pile forces.

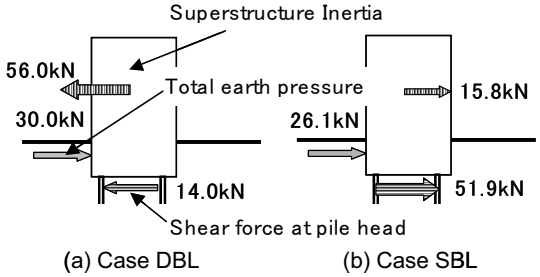

Fig. 16 Superstructure inertia, earth pressure and shear force at maximum bending moment

A method for estimating the phase between superstructure inertia and total earth pressure has been proposed by Tamura et al. (2002), based on the natural period of the superstructure under fixed footing condition T_b, the predominant period of the ground T_g, the soil displacement ΔS, and the footing displacement ΔB as shown in Fig. 17.

a) If $T_b < T_g$ and $\Delta S > \Delta B$, the total earth pressure tends to be in phase with the superstructure inertia (Fig. 17 (a)). Thus, the bending moment at the pile heads increases due to the total earth pressure.

b) If $T_b > T_g$ and $\Delta S > \Delta B$, the total earth pressure tends to be out of phase by 180 degrees with the superstructure inertia (Fig. 17 (b)). Thus, the bending moment at the pile heads decreases due to the total earth pressure.

c) If $T_b < T_g$ and $\Delta S < \Delta B$, the total earth pressure tends to be out of phase by 180 degrees with the superstructure inertia (Fig. 17 (c)). Thus, the bending moment at the pile heads decreases due to the total earth pressure.

d) If $T_b > T_g$ and $\Delta S < \Delta B$, the total earth pressure tends to be in phase with the superstructure inertia (Fig. 17 (d)). Thus, the bending moment at the pile heads increases due to the total earth pressure.

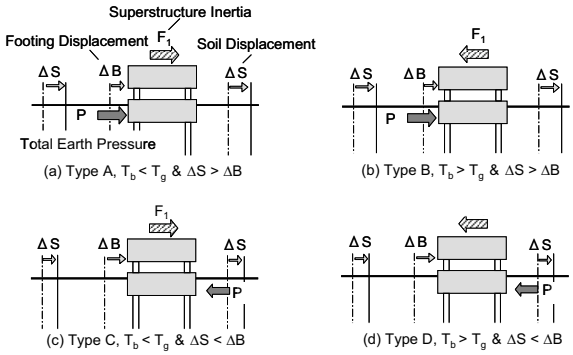

Fig. 17 Phase difference between total earth pressure and superstructure inertia (Tamura et al. 2002)

To investigate the effects of the total earth pressure on the bending moment at the pile head, the phase between the total earth pressure and the superstructure inertia in cases DBL and SBL are shown in Fig. 18. The data fallen in the first and third quadrants show that the total earth pressure tends to be in phase with the superstructure inertia, while those in the second and fourth quadrants show that the total earth pressure tends to be out of phase by 180 degrees with the soil inertia. A gray line in the figure shows that the soil displacement ΔS is smaller than the footing displacement ΔB, while a black line shows that ΔS is larger than ΔB.

In case DBL, most of the test data fall in the second and fourth quadrants. This indicates that the total earth pressure is out of phase by 180 degrees with the superstructure inertia. A black line is dominant, indicating that ΔS tends to be larger than ΔB when the total earth pressure reaches its peak. Considering that T_b is longer than T_g, conditions in case DBL corresponds to Type B in Fig. 17. The expected phase

between the superstructure inertia and the total earth pressure agrees with the test result.

In case SBL, the total earth pressure tends to be out of phase by 180 degrees with the superstructure inertia until 8 seconds. The phase is similar to that in case DBL. The total earth pressure, which is equivalent to about 60-70 percent of the superstructure inertia, counteracts the inertial force transmitted from the superstructure to the pile heads. It is unclear whether ΔS is larger than ΔB or ΔS is smaller than ΔB.

The relations between the two changed after 8 seconds, significantly. The total earth pressure tends to be in phase with the superstructure inertia. ΔS tends to be larger than ΔB when the total earth pressure reaches its peak. In addition, T_b is shorter than T_g due to the liquefaction. These conditions correspond to Type A in Fig. 17. The method as shown in Fig. 17 gives a reasonable explanation of the difference in earth pressure between the different tests.

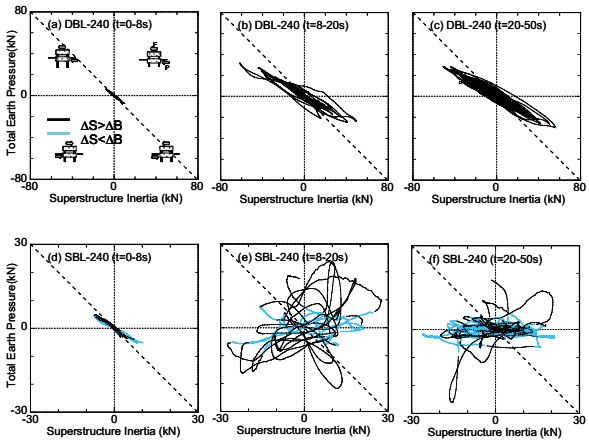

Fig. 18 Relation between superstructure inertia and total earth pressure

5.4 Conclusion

This paper examines earth pressure acting on an embedded footing and its effects on pile forces, based on both liquefaction and non-liquefaction tests using a large-scale laminar shear box. The following conclusions are drawn:

a) The total earth pressure in the non-liquefaction tests tends to be out of phase by 180 degrees with the superstructure inertia, reducing the shear force and bending moment at the pile head.

b) The total earth pressure in the liquefaction tests tends to be in phase with the superstructure inertia, making the bending moment at the pile head large. The proposed method gives a reasonable explanation of the difference in earth pressure between the different tests.

6. Methodologies for Life-Cycle Cost Estimation for Large-Scale Lifetime Network

6.1 Introduction

Seismic reliability analysis is necessary to estimate life-cycle cost for lifeline systems. However, it is a serious problem to count all system states of a large lifeline network in evaluating seismic reliability, because the number of system states increases exponentially with the number of the components. We propose a new method for evaluating seismic reliability of a large lifeline.

6.2 Definition of seismic reliability of a lifeline considering earthquake scenarios

In order to estimate the seismic reliability of a lifeline system we should consider various earthquake scenarios. The reliability is defined as,

$$R = \frac{\sum_{i=1}^{N} w_i \cdot f_i}{\sum_{i=1}^{N} w_i}, \qquad (1)$$

where, w_i is the weight for the earthquake scenario i, f_i the connectivity probability (probability for existing a path from the source node to sink node), N the number of earthquake scenario considered.

The analysis can be separated into 2 processes: evaluation of failure probability of network components for an earthquake scenario and evaluation of connectivity probability in the network system.

6.3 Method to evaluate failure probability of network components for an earthquake scenario

Firstly we assume that the ground motion for an earthquake scenario can be expressed by the distance from the site considered to an asperity centroid on the source fault. we call the distance *Xas* hereafter.

Equivalent hypocentral distance *Xeq* is defined as the distance from the site to the virtual point source which represent the fault plane with the distribution of energy released. (Ohno et al. 1993) It means that *Xeq* depends on the earthquake scenarios. We examine the relationship between *Xeq* and *Xas* for various earthquake scenarios and find that the relationship can

be approximated by a linear function as

$$Xas = \mathrm{a}\,Xeq + \mathrm{b} \tag{2}$$

Peak Ground Acceleration (PGA) is used as index of ground motion to estimate the damage ratio of network components. The following attenuation formula based on *Xeq* is used to estimate PGA.

$$PGA = 0.288Mw - 0.786\log Xeq - 0.00358Xeq + 1.62 \tag{3}$$

Secondly failure probability of an network component, P_f, is evaluated. The damage ratio of a component, *D*, is estimated from the following empirical formula (Isoyama et al. 1998);

$$D = C \times 4.58 \times 10^{-7} \times (PGA - 100)^{1.93} \tag{4}$$

where, C is coefficient determined from the pipe and site information. Note that *D* represents the averaged number of damage on a link per 1 km. The average damage number of the link with the length *L* [km] can be obtained as *LD*.

By assuming Poisson's process, we can calculate P_f of the link as follows;

$$P_f = 1\text{-}\exp(\text{-}LD)\ . \tag{5}$$

From Eq.(2) to (5), the relationship between P_f and *Xas* can be obtained (*Xas*→*Xeq*→PGA→*D*→P_f).

Finally, we can draw the counter lines on the source fault which show the location of asperity centroid giving the same P_f for a link as shown in Fig.19. Note that each location of asperity centroid represents an earthquake scenario.

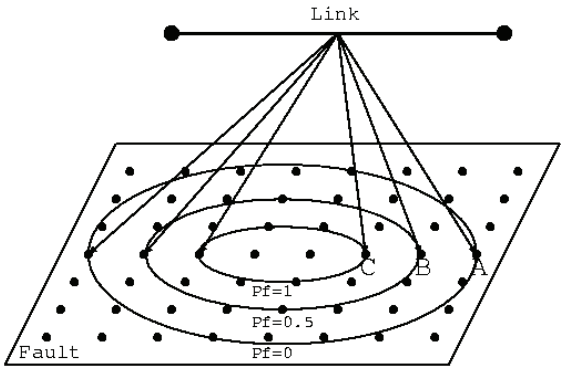

Fig. 19 P_f Counter lines of a link

6.4 Method to evaluation the connectivity probability in network system

All the system states must be considered to obtain exact solution of connectivity probability. As the number of system states increases exponentially with the number of the components, it becomes impossible to consider all system states by the limited CPU power. Monte Carlo method gives an approximated solution from the limited system states. It is well know that if we can sample the system states effectively, the CPU time for the analysis may decrease. We propose a new effective method to sample the system states.

A very simple network, shown in Fig.20, is used to explain the proposed method. Link failure is only considered for simplicity. All system states of the network are shown in Table 1. In the table, the cross mark means that the link is broken.

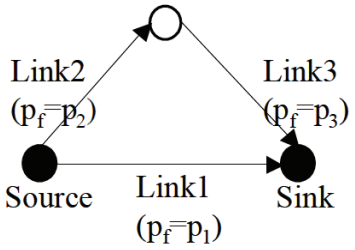

Fig. 20 Simple network

Table 1 All system states for the network

State	Link1	Link2	Link3	Connectivity
1	○	○	○	○
2	×	○	○	○
3	×	×	○	○
4	×	○	×	○
5	×	×	○	×
6	○	×	×	○
7	×	○	×	×
8	×	×	×	×

Assume that we sample 5 system states from the top line (states 1 to 5). From the sampled connective system states (states 1 to 4) we can calculate lower bound of the connectivity probability of network system $f_{\min}$. On the other hand, the sampled disconnective system state (state 5) gives the upper bound of the probability $f_{\max}$, as follows;

$$f_{\min} = P_1 + P_2 + P_3 + P_4 \quad , \tag{6}$$

$$f_{\max} = 1 - P_5 \quad . \tag{7}$$

where P_i is the occurrence probability of state *i*. The

exact solution f must exist between f_{min} and f_{max}, as

$$f_{min} < f < f_{max} \quad . \tag{8}$$

The proposed method samples the system states on the basis of the P_f contour line on the source fault obtained in the previous section. Fig.21 shows the counter lines of P_f=0.5 for all links in Fig. 20. The fault is divided into 8 regions by the counter lines. If the asperity centroid is located in region 6, failure probability of link 1 is less than 0.5 and those of link 2 and 3 are greater than 0.5. Consequently the most probable state in region 6 is the state that link 1 survives and link 2 and 3 fail. In other words, each region can represent a probable system state respectively. Note that the divided region on the fault is given by n^2-n+2, where n is the number of network components. Then the proposed method can sample the limited number of system states whose probability is large, and gives the upper and lower bound of connectivity probabilities..

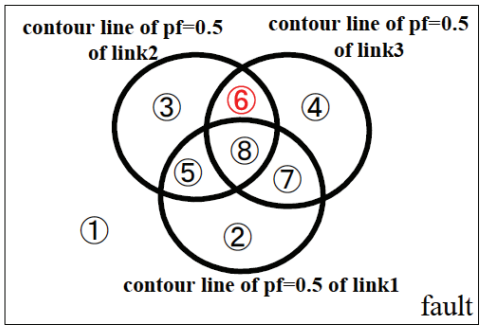

Fig. 21 Counter lines (P_f=0.5) for 3 links

If the earthquake scenario is changed, the probable connectivity pattern is changed but the division of the fault is not changed. The area of the region is used for the weight of the earthquake scenario, if the asperity centroid is located on the fault randomly.

Acknowledgements

We use data of K-NET, KiK-net strong motion network data. Several figures are made using GMT (Wessel and Smith, 1995).

References

AIJ Standard for structural calculation of reinforced concrete structures based on allowable stress concept (1999). Architectural Institute of Japan, 101-241 & 287-334.

Asano, K. and Iwata, T. (2006). Source process and near-source ground motions of the 2005 West Off Fukuoka Prefecture earthquake, Earth Planets Space, 58, 93-98.

Design and construction guidelines for multiple story frame structures with shear wall. (1999). The building center of Japan, 9-54 & 79-334

Isoyama, K., et al. (1998). Empirical formulation of damage-ratio based on Hyogoken-Nanbu darthquake, Tenth Japan Earthquake Engineering Symposium, 3175-3180 (in Japanese).

Matsumiya, T., Suita, K., Nakashima, M., Liu, D., Inoue, M., and Takehara, S. (2004). Effect of ALC panel finishes on structural performance – test on full-scale three story steel frame for evaluation of seismic performance –“, Journal of Structural and Construction Engineering, The Architectural Institute of Japan, 581, 135-141 (in Japanese).

Midorikawa, M., Okawa, I., Iiba, M., and Teshigawara, M. (2003). Performance-based seismic design code in Japan. Earthquake Engineering and Engineering Seismology, Taiwan, 4(1), 12−25.

Miyake, H., Iwata, T., and Irikura, K. (2003). Source characterization for broadband ground-motion simulation: Kinematic heterogeneous source model and strong motion generation area, Bull. Seism. Soc. Am., 93, 2531-2545.

Nakamichi, S. and Kawase, H. (2002). Broadband strong motion simulation in Fukuoka City based on a three-dimensional basin structure and a hybrid method, J. Struct. Constr. Eng., AIJ, 560, 83–91 (in Japanese).

Nakashima, M., Akazawa, T., and Igarashi, H. (1995). Pseudo dynamic testing using conventional testing devices. Journal of Earthquake Engineering and Structural Dynamics, 124(10), 1409-1422.

Nakashima, M., Inoue, K., and Tada, M. (1998). Classification of damage to steel buildings observed in the 1995 Hyogoken-Nanbu Earthquake. Engineering Structures, 20(4), 271-281.

Nakashima, M., and Liu, D. (2005). Instability and complete failure of steel columns subjected to cyclic loading. Journal of Engineering Mechanics, ASCE, 131(6), 559-567.

NEHRP Recommended Provisions for Seismic Regulations for New Buildings and Structures.

(2000). FEM368, Federal Emergency Management Agency, Building Seismic Safety Council,, Washington DC.

Notification No.1457-2000, Technical Standard for Structural Calculation of Response and Limit Strength of Buildings. (2000). Ministry of Land, Infrastructure and Transport (in Japanese).

Ohno, S. et al. (1993). Revision of attenuation formula considering the effect of fault size to evaluate strong motion spectra in near field. Tectonophisics, 218, 69-81.

Paulay, T. and Priestley, M. J. N. (1992). Seismic design of reinforced concrete and masonry buildings, John Wiley & Sons, 362-499.

Performance-Based Seismic Engineering of Buildings. (1995). SEAOC Vision 2000 Committee, Structural Engineers Association of California, Sacramento CA.

Reconnaissance Report on Damage to Steel Building Structures Observed from the 1995 Hyogokken-Nanbu Earthquake. (1995). Steel Committee of the Kinki Branch of the Architectural Institute of Japan, Osaka (in Japanese).

Somerville, P., Irikura, K., Graves, R., Sawada, S., Wald, D., Abrahamson, N., Iwasaki, Y., Kagawa, T., Smith, N., and Kowada, A. (1999). Characterizing crustal earthquake slip models for the prediction of strong motion, Seism. Res. Lett., 70, 59–80.

Suzuki, W. and Iwata, T. (2006). Source model of the 2005 west off Fukuoka prefecture earthquake estimated from the empirical Green's function simulation of broadband strong motions, Earth Planets Space, 58, 99-104.

Tamura, S., Tokimatsu, K., Uchida, A., Funahara, H. and Abe, A.(2002). Relation between seismic earth pressure acting on embedded footing and inertial force based on liquefaction test using large scale shear box", Journal of Struct. Constr. Engng., 559, 129-134. (in Japanese)

Tamura, S., Tsuchiya, T., Suzuki, Y., Fujii, S., Saeki, E. and Tokimatsu, K. (2000). Shaking table tests of pile foundation on liquefied soil using large-scale laminar Box (Part 1: Outline of Test). 35th Japan National Conference on Geotechnical Engineering, 1907-1908. (in Japanese)

Tokimatsu, K., Suzuki, H. and Sato, M. (2004). Influence of inertial and kinematic components on pile response during earthquake, Proc. of 11th International Conference on Soil Dynamics and Earthquake Engineering & 3rd International Conference on Earthquake Geotechnical Engineering, Berkeley, 1, 768-775.

Wessel, P. and Smith, W. H. F. (1995). Free software helps map and display data, EOS, 72, 441, 445–446. estimated from the empirical Green's function simulation of broadband strong motions, Earth Planets Space, 58, 99-104.

多次元評価手法の統合化による都市施地震脆弱性診断手法の高度化

中島正愛、田中仁史、岩田知孝、澤田純男、松波孝治、吹田啓一郎、田村修次

要旨

都市に存在する多くの構造物の地震時における脆弱性を合理的に評価するためには、構造物の供用期間、地震時に作用する外力、それに対する性能と損傷進展、被害やその復旧に要する費用、維持管理に要する費用などを総合的に評価する必要がある。本主題による5年間の研究のうち、本年度においては、福岡県西部地震における観測記録等を用いた強震動予測手法の洗練、建物における非構造部材が有する耐震性能の把握、建物基礎と上部構造の連成を考慮した耐震性能評価法の提案、地耐力が杭基礎に及ぼす効果の検証、大規模ライフライン網に対する簡便なライフサイクル評価方法の提案を骨子として研究を展開した。

キーワード： 強震動、非構造部材の性能、基礎－構造系相関、杭への地耐力、ライフサイクルコスト